

Article

Numerical Seismic Fragility Analysis of Glass Curtain Walls: Gaps and Challenges in Modelling Optimization and Limit Performance Indicators

Nicola Cella  and Chiara Bedon * 

Department of Engineering and Architecture, University of Trieste, 34127 Trieste, Italy; nicola.cella@phd.units.it
* Correspondence: chiara.bedon@dia.units.it; Tel.: +39-040-558-3937

Abstract: Glass facades are known to be fascinating building systems that require specific design strategies, experimental protocols and simulation tools. Especially for seismic-resistant buildings, their mechanical performance should be verified against possible failure mechanisms. For this, both numerically optimized and robust approaches are needed, along with tools to support designers. Fragility curves represent, in this sense, a practical approach for many structural typologies and systems. In this paper, attention is given to the development and assessment of a geometrically simplified and mechanically optimized FE numerical model for the non-linear dynamic analysis of glass curtain walls (GCWs). Its potential and gaps in its calibration and prediction capacity, both at the global and local level, are addressed on the base of earlier experimental and numerical studies. A fragility analysis is then carried out by taking advantage of the cloud analysis method to verify the real capacity of a typical GCW and the performance restrictions that are presently recommended by existing standards for construction. A total of 60 non-linear dynamic analyses are carried out for GCWs under real seismic acceleration to capture the maximum effects and possible failure mechanisms. An analysis of the parametric results is then carried out for several performance indicators of practical interest and various technical documents of the literature. As shown, there is a major effect of global and local mechanisms that optimized numerical models should properly capture. At the same time, according to existing technical documents, there is a clear need for more efficient limit values and performance indicators for the design of safe and optimized seismic-resistant GCWs.



Citation: Cella, N.; Bedon, C. Numerical Seismic Fragility Analysis of Glass Curtain Walls: Gaps and Challenges in Modelling Optimization and Limit Performance Indicators. *Buildings* **2024**, *14*, 3863. <https://doi.org/10.3390/buildings14123863>

Academic Editor: Xavier Romão

Received: 9 November 2024

Revised: 27 November 2024

Accepted: 28 November 2024

Published: 30 November 2024



Copyright: © 2024 by the authors. Licensee MDPI, Basel, Switzerland. This article is an open access article distributed under the terms and conditions of the Creative Commons Attribution (CC BY) license (<https://creativecommons.org/licenses/by/4.0/>).

Keywords: glass curtain walls (GCWs); finite element (FE) numerical modelling; fragility curves; cloud analysis; seismic performance

1. Introduction

Glass curtain walls (GCWs) are becoming an increasingly popular component in modern architectural buildings, due to their aesthetic appeal. Commonly, GCWs consist of a structural frame, usually made of aluminium, anchored to the load-bearing structure of the building by means of connections at the floor levels. The frame supports infill glass panels that are used to create a continuous envelope which is expected to fulfil all the basic functions of an external wall and a physical barrier. From a structural design perspective, these systems are not intended to largely contribute to the load bearing of the primary building structure and are therefore classified as “non-structural elements” by most common standards for building design. The major issues pertaining to structural safety are attributable to the intrinsic brittle behaviour of glass, which makes GCWs highly vulnerable to ordinary and accidental loads and poses a significant risk to the occupants, particularly when subjected to extreme loads [1].

When subjected to earthquakes, for example, GCWs are highly susceptible to damage in their constituent components, as a major consequence of an intrinsic incompatibility between the inter-storey relative displacements of the primary structure (i.e., the building) and the deformation capacity of the facade. To address these important aspects and

mechanisms, Sucuoğlu and Vallabhan [2] proposed a simple schematization of the problem. Basically, the inter-storey drift leads to a rigid translation of the glass panel within the frame until the glass–frame clearance closure. The contact occurs at two opposite corners and the panel starts an in-plane rotation. The glass panel rotates until the corners coincide with those of the frame or, in other terms, the shorter diagonal of the frame is equal to that of the glass panel. In this final configuration, the infill glass panel behaves like a strut and may collapse due to compression (crushing) or loss of support at the edges, with the sound panel consequently falling down.

Currently, the reference approach to assess the behaviour of a facade subjected to seismic action consists in experimental tests on full-scale samples, as also prescribed by [3,4]. Such an approach, however, is clearly expensive and time-consuming. Therefore, several standards propose to account for a simplified calculation approach, which is based on the limitation of the inter-storey drift (IDR) of the primary structure to avoid the damage of “non-structural elements” [5,6]. Unfortunately, the reference IDR limitations are provided for generic non-structural infills only, which are not appropriate for GCWs, and thus they can lead to a non-optimal design. For this reason, specific IDR limitations are needed for glass facades or, alternatively, a reliable and sufficiently refined finite element (FE) numerical strategy should be developed to assist designers in the seismic assessment of GCWs. In this regard, the potential of FE numerical tools to reduce the need for full-scale tests is becoming increasingly evident and has been corroborated by successful applications of FE modelling strategies for the numerical analysis of several configurations of GCWs subjected to seismic loads [7–10]. However, due to the basic complexity of GCW systems, a very high numerical accuracy is commonly required to capture the mechanical interaction of primary and secondary GCW components under seismic events. On the other side, the intrinsic need for FE models with a high computational efficiency suggests the elaboration of major simplifications in the model assembly, and further research efforts are hence required.

For all the above considerations, the present study aims to develop and present an enhanced but geometrically simplified numerical approach that can be efficiently used to predict the in-plane seismic performance of a traditional stick system. In order to achieve this objective, a previously investigated GCW [10,11] is considered and briefly described in Section 2. The proposed modelling strategy, which is presented in more detail, draws inspiration from earlier extended numerical efforts [10,11] and seeks to overcome the need for experimental data to calibrate robust FE numerical assemblies. A comprehensive and detailed description for the adopted modelling approach is proposed in Section 3.1. Successively (see Section 3.2), the in-plane seismic performance of the reference FE numerical model is validated (both at the global and local levels) against the experimental dataset provided in [10]. Finally, based on the newly developed FE model, a fragility analysis is presented in Section 4. As shown in Section 4.1, the use of a cloud analysis in Cornell’s reliability method implicitly confers a significant advantage for the purpose of the present study. This analytical method provides in fact a means of investigating a given structure, taking into account variations in seismic motions and uncertainties in structural parameters. In the context of a fragility analysis, Sections 4.2 and 4.3 focus on the definition of a suitable set of input ground motions and engineering demand parameter (EDP) thresholds, which are calibrated according to available standards. The major outcomes from the parametric numerical analyses are discussed in Section 4.4. Finally, fragility curves are derived in Section 4.5, with a sound discussion of comparative results, based on the selected performance indicators.

2. Reference GCW System and Experimental Protocol

For the present study, the facade (and experimental setup) presented in [10,12] and already numerically investigated in [11] with a full 3D solid numerical model was taken into account.

The facade, a 7.80 m × 5.38 m stick system (Figure 1a), is characterised by a supporting frame composed of five mullions and twenty transoms in extruded aluminium (alloy EN-AW 6060, supply type T5), mutually connected by a U-bolt rail system. The infill glass panels, which are 1300 mm × 1900 mm, consist of insulating glass units (IGUs) composed of two laminated layers separated by a 16 mm cavity. The two layers are made up of two 4 mm thick annealed glass plates bonded with two 0.38 mm thick PVB foils. Thus, the IGU-resistant section is 44.2/16/44.2. Moreover, each IGU is supported by two aluminium plates (setting blocks) with a layer of plastic material (rubber pads) on top (Figure 1d) placed at the ends of transoms and held in position by means of aluminium pressure plates screwed to the frame (Figure 1c). As shown in Figure 1c, the clearance between each IGU and the frame is 6 mm.

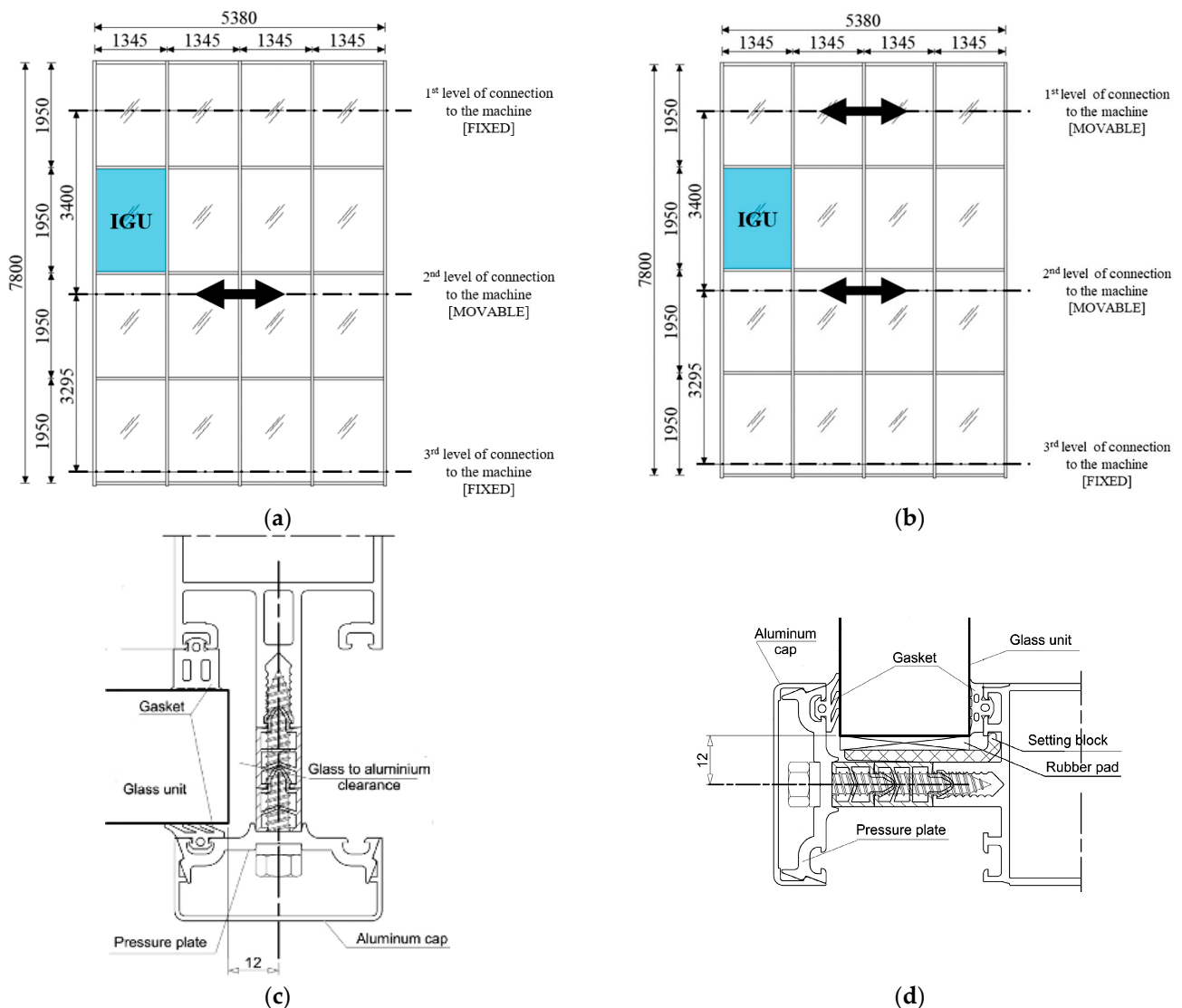


Figure 1. Reference system: (a) Test “VI” setup, (b) Test “XI” setup, (c) glass-to-mullion and (d) glass-to-transom details (dimensions in mm).

For the original experimental investigation in [10], the frame was fixed to the test apparatus at three different levels, as shown in Figure 1. The reference facade from [10] was then subjected to a series of eleven in-plane cyclic tests, both static and dynamic, carried out under displacement control. For the purpose of the present numerical study, the tests “VI” and “XI” from [10] were specifically taken into account.

The former (Test “VI”) consisted of a quasi-static sequence of horizontal displacements, applied to the movable intermediate beam of the test facility at a constant velocity of 1 mm/s (Figure 1a). Each series of displacements reached progressively higher peak values, as shown in Figure 2a, with a maximum of 45 mm (corresponding to an inter-storey drift ratio of approximately 1/75). The latter (Test “XI”) corresponded to a dynamic racking crescendo protocol, consisting of a series of sinusoidal cycles, made up of alternating intervals of constant and increasing maximum displacement (four sinusoidal cycles each), with a displacement step of 6 mm. The imposed displacement was applied to the two upper movable beams in opposition of phase, as shown in Figure 1b. Within the scope of the present investigation (see also Section 4), the numerically applied in-plane lateral displacement is described in Figure 2b, limited to the maximum amplitude of interest for the cloud analysis. This choice was selected to properly validate the dynamic response of the assembled FE model (i.e., components, connectors and materials) with explicit reference to the range of displacements of interest for the parametric seismic analysis, rather than a general validation up to the point of collapse. In this regard, it is worth noting that no glass breakage occurred for tests “VI” and “XI” considered in the experimental analysis of [10].

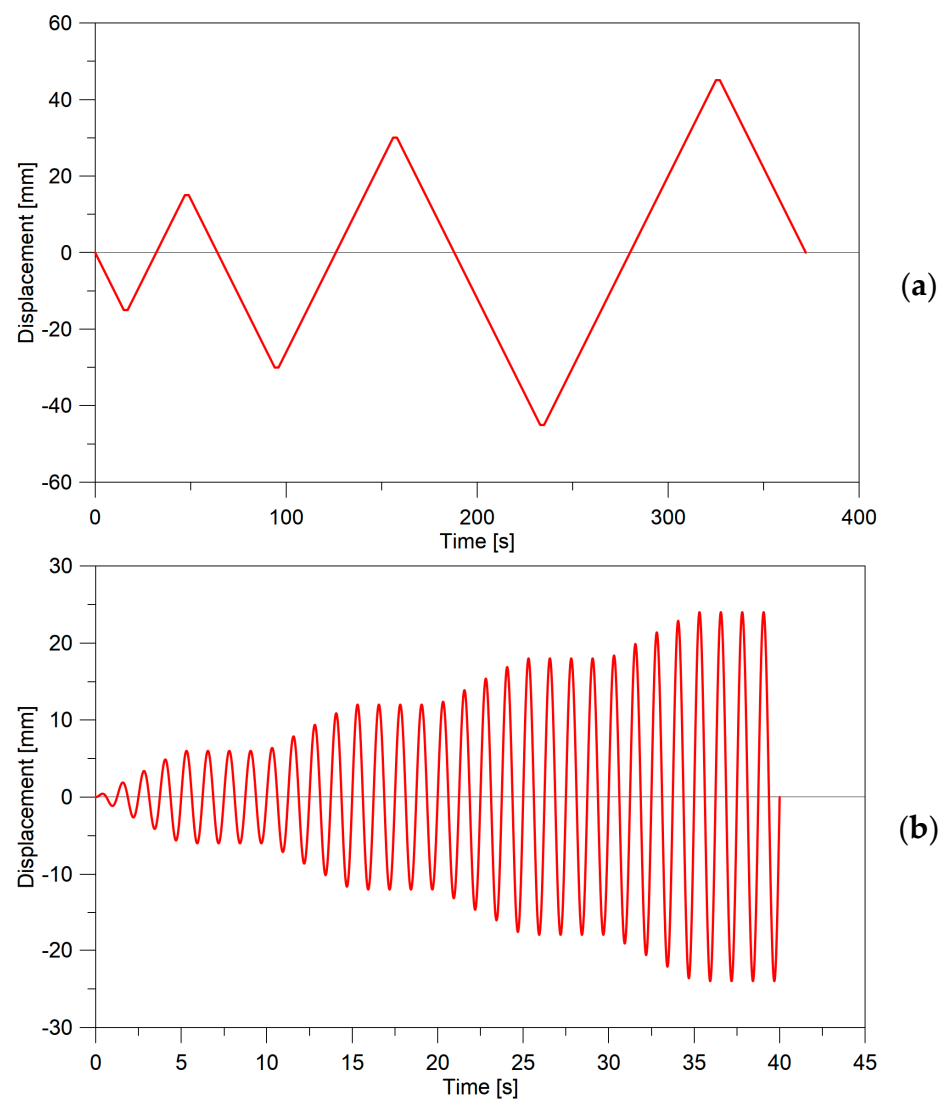


Figure 2. Reference displacement time histories for the present numerical study (based on the experimental setup discussed in [10]): (a) Test “VI” (full protocol) and (b) Test “XI” (limited to 40 s).

3. Finite Element Numerical Analysis

3.1. Numerical Modelling

For the purpose of the present study, an original, geometrically simplified numerical model was implemented in ABAQUS v. 6.14 [13]. For this aim, we capitalized on the most notable advantages of the extended numerical studies reported in [10,11]. For major differences from the previously adopted modelling approaches [10,11], see Table 1. The present numerical model consisted of 2D shell elements to accurately represent the geometrical features of the aluminium frame, which were preferred to generic and roughly simplified 1D beam elements (with nominal section properties). Different types of connectors were also employed, see Figure 3. According to [10], transoms were assumed to be hinged at both ends by means of a *Hinge*-type connector [13]. This type of connector joins the position of two nodes and provides a revolute connection between their rotational degrees of freedom (DOFs). In detail, the *Hinge*-type connector keeps the relative position of the two connected nodes fixed ($U_1 = U_2 = U_3 = 0$) and constrains the rotations in two local directions ($UR_2 = UR_3 = 0$), while the rotation in the connector local 1 direction (UR_1) is free. The latter was set to be coincident with the major principal axis of the transom.

Table 1. Basic features of present modelling strategy, compared to [10,11], for the selected GCW system. * = 1/4th facade only. Analysis = 1: quasi-static monotonic; 2: quasi-static cyclic; 3: crescendo test; 4: non-linear dynamic with base accelerometer.

Model	Facade Components				Model Size		Analysis
	IGUs	Frame	Gaskets	Setting Blocks	DOFs	Elements	
Present	2D shell	2D shell	Connectors	Connectors	245,870	41,387	1, 2, 3, 4
MREF [11] *	3D brick	3D brick	3D brick	3D brick	1,509,750	430,876	1
MSIMP [11]	2D shell	1D beam	Connectors	Connectors	8308	2589	1, 2
Aiello et al. [10]	2D shell	1D beam	Connectors	Connectors	N/A	N/A	2, 3

Two-dimensional shell elements were also used to describe the IGUs, in the form of monolithic elements with total thickness equal to the sum of glass layers only (and thus disregarding the presence of the cavity, PVB layers and edge spacer connections). This assumption typically results in a major simplification compared to accurate IGU models [14,15], but—as shown in the present setup—it can correctly capture the resisting mechanisms of the examined GCW under in-plane seismic loads. In particular, special attention was given to the description of local contact mechanisms. As such, for the shell elements representing the glass panes of IGUs, a section offset was taken into account, and the principal plane of 2D shell elements was placed to coincide with the inner surface of the IGUs, thereby representing the actual location of the contact between the glass and the frame [11].

As in [10,11], two connectors were employed in parallel to reproduce the mechanical interaction between the different components of the facade (Figure 4c). In detail, a *Cartesian*-type connector was first used to represent any contact between IGUs and frame members, following clearance closure. This effect was achieved by defining a non-linear elastic behaviour in the direction of connector axis (Figure 3a). A second *Cartesian*-type connector was used to characterize the mechanical behaviour of gaskets. In this latter case (see Figure 3c,d), the in-plane elastic–plastic behaviour was separately defined for mullion and transom gaskets (to reproduce the mechanical response in the global x and y directions, as in Figure 4a). Finally, to account for the presence of pressure plates, the mechanical behaviour of the same connector in the out-of-plane direction was set as ideally *Rigid*.

In conclusion, the mechanical role of setting blocks was accounted for by introducing an *Axial*-type connector in the corresponding region. A non-linear elastic behaviour was assigned to each one of these connectors (Figure 3b) in order to reproduce the contact between the glass panels and the frame (for the GCW at rest) as well as any possible relative displacement and detachment for the GCW under in-plane seismic events.

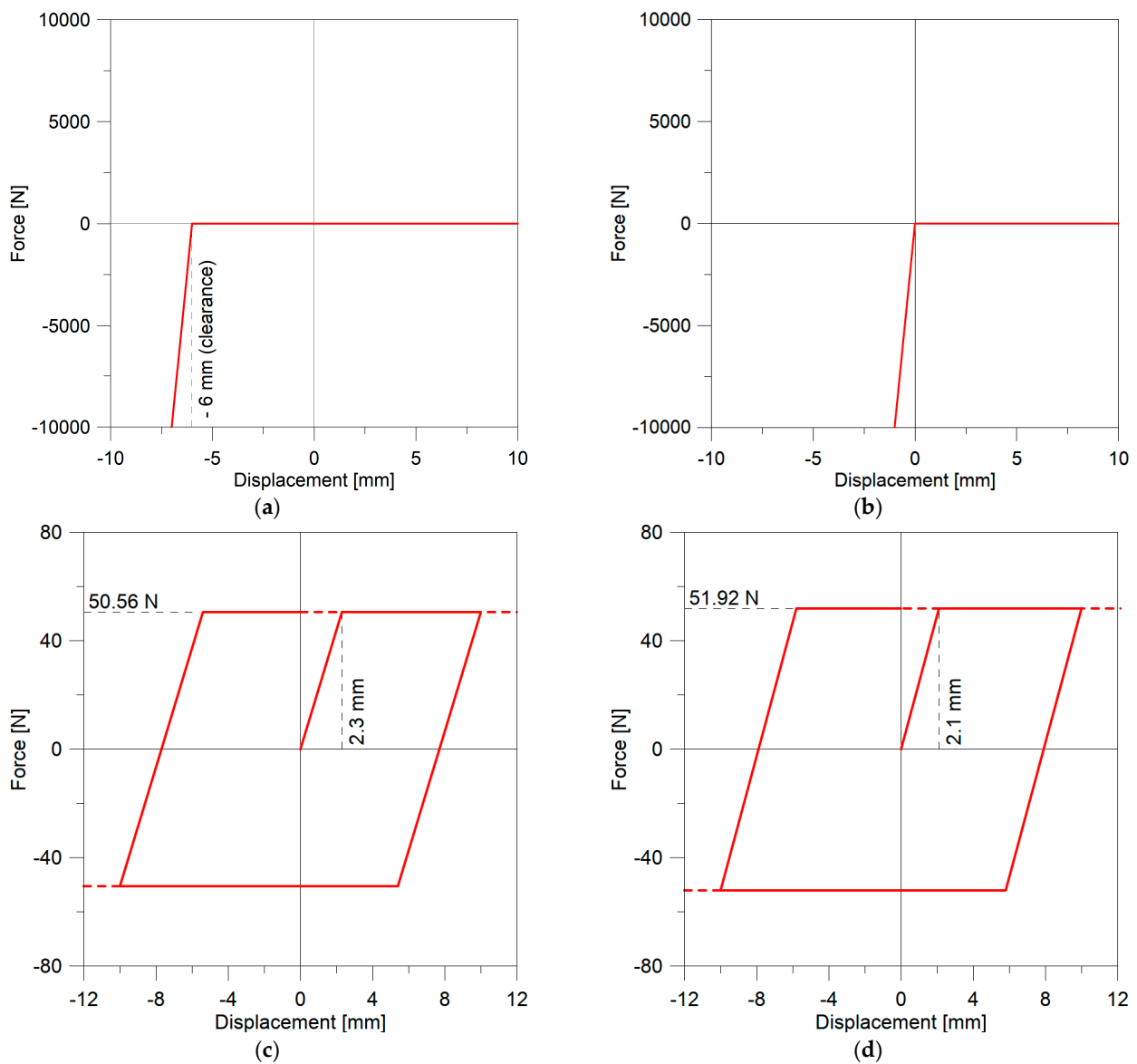


Figure 3. Non-linear connector behaviours: (a) contact following clearance closure, (b) setting blocks, (c) mullion gaskets and (d) transom gaskets.

It is important to note that for the EPDM gaskets, in contrast to previous approaches [10,11], a simple model inspired by the shear response of rubber seismic isolators was assumed in the present study, as also suggested by [12]. In detail, the plasticization of the gasket was assumed to occur for a shear strain in each gasket equal to its height (i.e., gasket thickness); see [12] for more details. It is also worth highlighting that, as shown in Figure 3c,d, a bilinear model was adopted even though the inner and outer gaskets (for both mullions and transoms) have a different height [12]. From a practical point of view, the elastic stiffness assigned to the reference connector can be calculated with the following equation:

$$k_g = G_g \cdot \sum_{i=1}^2 \frac{b_{g,i}}{h_{g,i}} \cdot l_g \quad (1)$$

where $G_g = 0.021$ MPa is the shear modulus of EPDM [12], $b_{g,i}$ and $h_{g,i}$ represent the width and height of the gasket cross section, respectively, and l_g is the spacing of connectors (see Figure 4b).

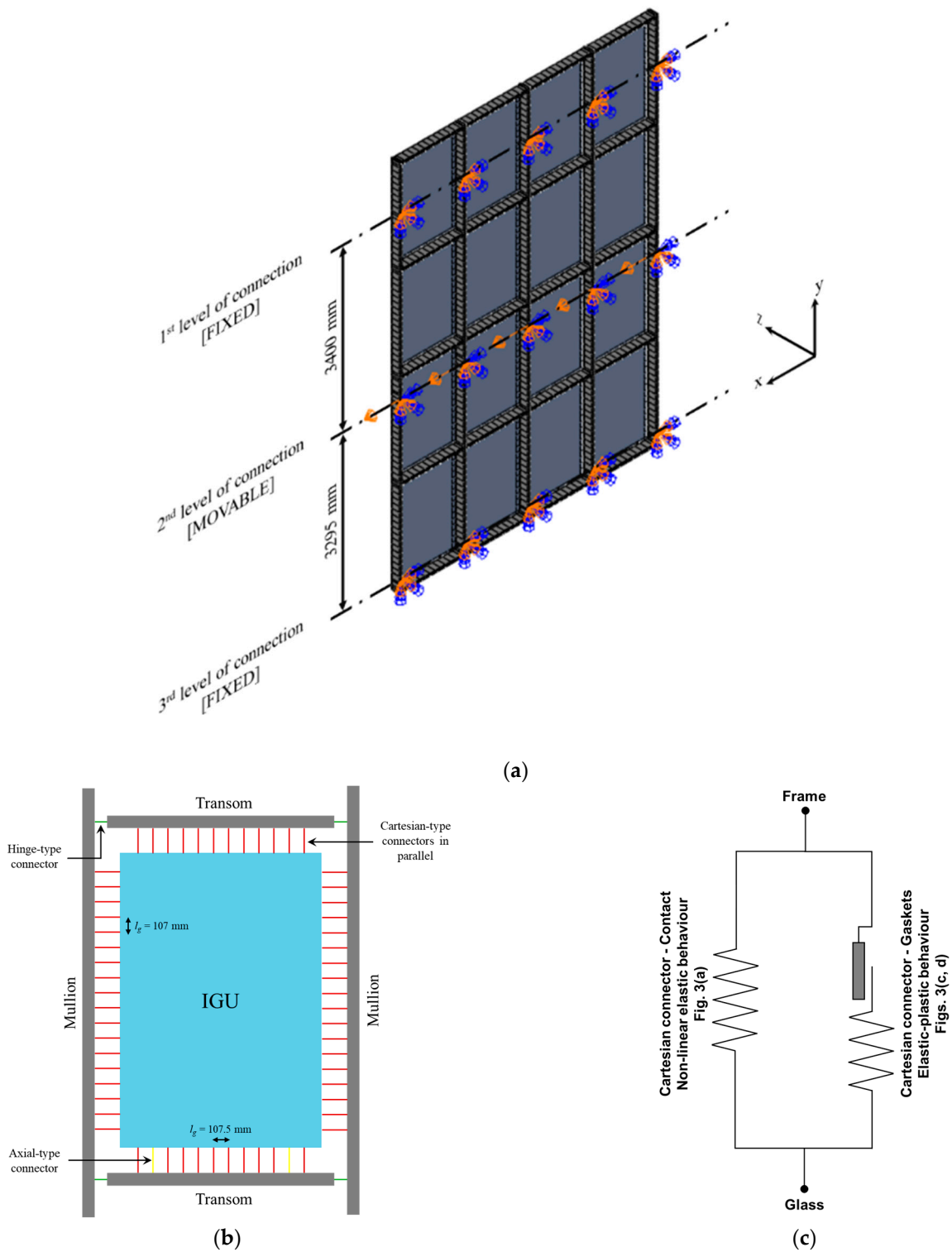


Figure 4. Present numerical model developed in ABAQUS v. 6.14: (a) 3D view of Test VI setup, (b) schematic representation of a facade module and (c) mechanical model for two connector elements working in parallel.

Similarly, the corresponding yield strength can be calculated as follows:

$$F_g = G_g \cdot \sum_{i=1}^2 b_{g,i} \cdot l_g \tag{2}$$

where the subscript $i = 1, 2$ stands for inner (1) or outer (2) gasket. The input parameters that were finally adopted for the typical gasket connector in the present study are summarized in Table 2.

Table 2. Gasket connector parameters.

Connector	$b_{g,1}$ [mm]	$h_{g,1}$ [mm]	$b_{g,2}$ [mm]	$h_{g,2}$ [mm]	l_g [mm]	k_g [N/mm]	F_g [N]
Mullion	11.0	11.5	11.5	1.3	107.0	22.0	50.56
Transom	11.5	5.5	11.5	1.3	107.5	24.7	51.92

With regard to the possible contact between IGUs and frame, the elastic stiffness assigned to the connectors was defined with the aim of reducing any relative displacement after their contact, as well as to avoid possible convergence problems. Therefore, the stiffness value was set almost two orders of magnitude higher than the numerically estimated value in the mid-span section (≈ 500 N/mm).

A schematic representation of the assembled FE model is shown in Figure 4a. The approximate global size of the mesh was set as 50 mm. This choice led to 39,459 shell elements (S4R type) and 245,870 DOFs. Regarding the connectors required to provide the mechanical interaction between the constituent GCW components, the adopted spacing resulted in 1928 elements (Figure 4b).

To reproduce the experimental setup and test protocol described in [10], the reference numerical simulation was defined as a “dynamic implicit” analysis in displacement control. The imposed in-plane lateral displacement for the GCW model was applied both monotonically (only for Test “VI”), with the same strain rate of the test in [10], as well as in accordance with the cyclic time histories shown in Figure 2. The different boundary conditions considered for the present numerical analyses are summarized in Table 3.

Table 3. Boundary conditions for the considered numerical setups.

Setup	Boundary Conditions			Load Type
	1st Level	2nd Level	3rd Level	
Test VI	$U_x = U_y = U_z = 0$ $U_{Rx} = U_{Ry} = U_{Rz} = 0$	$U_y = U_z = 0$ $U_{Rx} = U_{Ry} = U_{Rz} = 0$	$U_x = U_y = U_z = 0$ $U_{Rx} = U_{Ry} = U_{Rz} = 0$	Imposed displacement
Test XI	$U_y = U_z = 0$ $U_{Rx} = U_{Ry} = U_{Rz} = 0$	$U_y = U_z = 0$ $U_{Rx} = U_{Ry} = U_{Rz} = 0$	$U_x = U_y = U_z = 0$ $U_{Rx} = U_{Ry} = U_{Rz} = 0$	Imposed displacement
Fragility analysis	$U_y = U_z = 0$ $U_{Rx} = U_{Ry} = U_{Rz} = 0$	$U_y = U_z = 0$ $U_{Rx} = U_{Ry} = U_{Rz} = 0$	$U_y = U_z = 0$ $U_{Rx} = U_{Ry} = U_{Rz} = 0$	Input base accelerometer

Finally, the mechanical properties for annealed glass and aluminium were characterized based on product standards, thus resulting in elastic moduli of $E_g = E_a = 70$ GPa for glass and aluminium, corresponding Poisson ratios of $\nu_g = 0.23$ and $\nu_a = 0.30$, and nominal densities of $\rho_g = 2500$ kg/m³ and $\rho_a = 2700$ kg/m³, respectively. It is worth noting that a linear elastic constitutive law was taken into account for both glass and aluminium materials, since no failure occurred during the considered experimental test [10]. In addition, a damping of $\zeta = 1.5\%$ was taken into account by the Rayleigh method. The corresponding input Rayleigh damping factors resulted in $\alpha_g = \alpha_a = 0.055$ 1/s and $\beta_g = \beta_a = 0.003$ s.

3.2. Numerical Model Validation

3.2.1. Global Performance Assessment

Figure 5 shows a comparison between the experimental response from [10] and the results of the presently developed FE numerical model in ABAQUS v. 6.14 [13], in terms of monotonic and cyclic load–displacement curves (Test “VI”). The former (see Figure 5a) shows a quite good agreement with the experimental curve and therefore confirms that

the present numerical approach is able to predict the global seismic behaviour of similar stick systems. However, it is also important to remark that the recorded numerical force–displacement path of Figure 5a looks less resistant, compared to the experimental outcome, with a peak lateral force at maximum imposed displacement that is slightly smaller than that in the test (−3.1%). The high similarity in terms of GCW stiffness for the second branch of the force–displacement curve also suggests that the measured strength scatter can derive from a non-optimal description of gasket behaviour, which represents secondary components that are rather challenging and not easy to mechanically simplify, especially through discrete connectors.

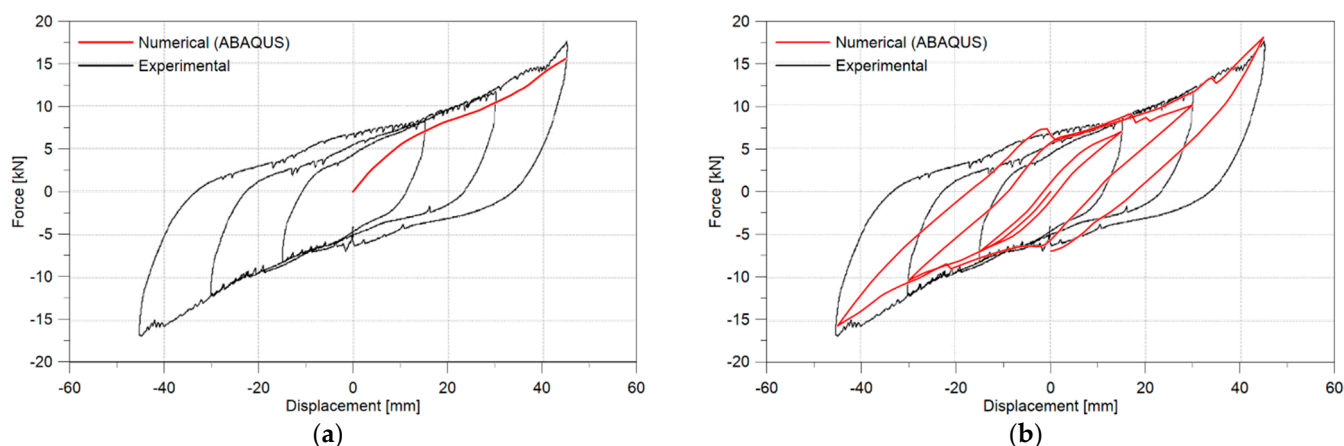


Figure 5. (a) Monotonic and (b) cyclic force–displacement response compared to the reference experiment (Test “VI”) [10].

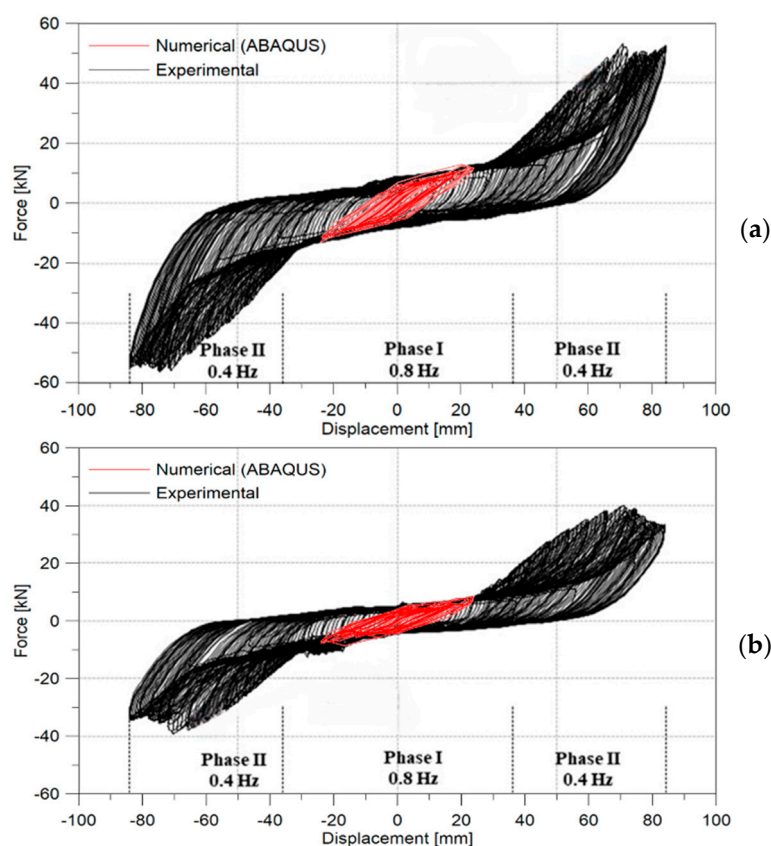
Similar discrepancies also emerge when comparing the cyclic response of experimental and numerical outcomes; see Figure 5b. Overall, the adopted simplified numerical strategy was sufficiently accurate to capture the global in-plane lateral response of the system, but was still associated with some variable scatter in the reproduction of the experimental energy dissipation, in particular, for the first imposed cycle.

Again, this partial inconsistency is related to the minimization of gaskets to discrete equivalent mechanical connectors. In this sense, further experimental tests could be helpful to further enhance the calibration of gaskets and thus develop a more reliable model. From the calculated scatter between experimental and numerical results, which is further detailed in Table 4 for each imposed cycle, it is in any case possible to observe the quite good level of agreement between the collected data, with an absolute mean error of about 12% for all the cycles. Only for the last one, the residual force value measured at the end of the test shows a remarkable error (+34.6%), which is in any case out of the range of interest for the parametric fragility analyses of this paper. Overall, the presented results suggest the potential applicability of the current modelling approach in time history analyses for global performance assessment purposes.

Finally, Figure 6 shows the comparison between the experimental and numerical results for Test “XI” [10]. As previously observed, only a limited part of the full experimental test was numerically replicated in this study. The reason for this was to evaluate and verify the dynamic performance of the reference FE model within the context of cloud analysis (Section 4). The satisfactory alignment of the obtained numerical curves with the experimental outcomes of Figure 6, as shown, further supports the validity of the present modelling approach for non-linear dynamic analysis purposes, when considering the range of displacements of interest.

Table 4. Comparison between experimental [10] and numerical absolute lateral force peaks, at different amplitudes of imposed displacement.

Displacement [mm]	Force [kN]		Difference [%]
	Experimental	Numerical	
+15	7.5	7.1	−5.3
−15	7.5	7.1	−5.3
+30	11.5	10.2	−11.3
−30	11.1	10.4	−6.3
+45	16.1	18.1	+12.4
−45	17.5	15.8	−9.7
0	5.2	7.0	+34.6

**Figure 6.** Cyclic load–displacement response for (a) intermediate (2nd level) and (b) upper beam (1st level) compared to the reference experiment (Test “XI”) [10].

3.2.2. Local Performance Assessment

In addition to global performance considerations, the local performance assessment of GCW systems and models is also of utmost importance for calibration and validation purposes. If the nominal geometry is simplified, local effects and resisting mechanisms could suffer as a consequence [11].

The deformed shape of the examined facade, at the maximum imposed lateral displacement of 45 mm, is shown in Figure 7. The deformed configuration for a selected IGU, as highlighted in Figure 7, shows that the adopted modelling strategy can efficiently replicate the translation and rotation of glass panels within the supporting frame when subjected to in-plane seismic actions [2]. In this regard, a comparison in terms of in-plane rotation is also reported in Figure 8, in which the behaviour of the same glass element is shown for both the numerical assemblies from [11] and the present approach. The good level of agreement

obtained with the MREF assembly (1.0% scatter at the maximum imposed displacement) highlights the ability of this approach to capture glass–frame interaction.

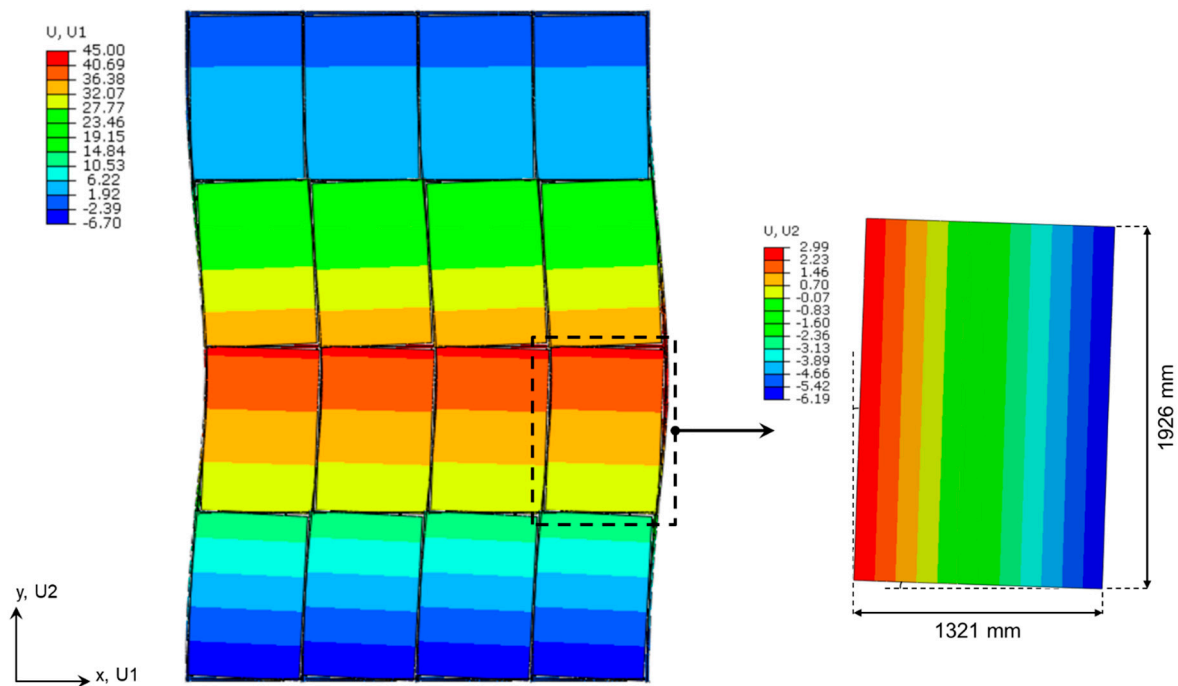


Figure 7. Deformed shape at the imposed displacement of +45 mm: contour plot of displacement components along U1 and U2 directions (scale factor = 5, values in mm).

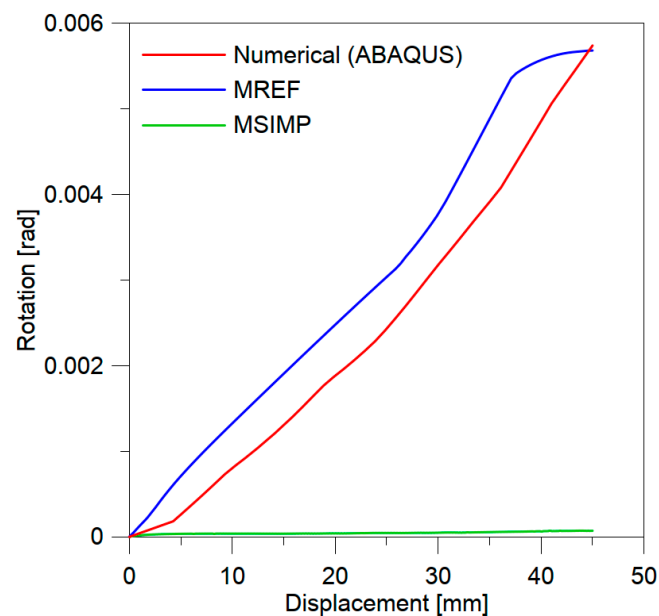


Figure 8. Rotation of a glass element as a function of the imposed in-plane lateral displacement compared to MREF and MSIMP [11].

Finally, attention was paid to the stress evaluation of IGUs. In fact, it is well recognized that the correct assessment of stress peaks in glass components is of primary importance to verify possible failure mechanisms. In this regard, Figure 9 shows the compressive principal stress distribution that was numerically obtained in the most stressed glass element, when subjected to an in-plane lateral displacement of +45 mm. Due to the contact with the frame, the selected IGU in Figure 9 clearly shows a compression strut along the

diagonal, with stress peaks at two opposite corners, which is also in accordance with [11] and with the typical response described in [2]. In contrast to the results obtained with the MREF model in [11], the maximum compressive stress was numerically recorded in the region of the compressed setting block, and not at the corner in direct contact with the frame. Moreover, the principal stress peaks resulted in approximately 6 MPa in tension and 12 MPa in compression, which are remarkably lower compared to the values recorded in [11]. This difference in stress predictions could represent the major limitation of this simplified numerical approach for conservative design considerations at component level. However, it is also important that it is not possible to correctly assess the scatter of stress evaluations because of the lack of local experimental measurements [10]. For this reason, further experimental evidence is certainly needed to assess the reliability of the model for the local performance assessment of the system.

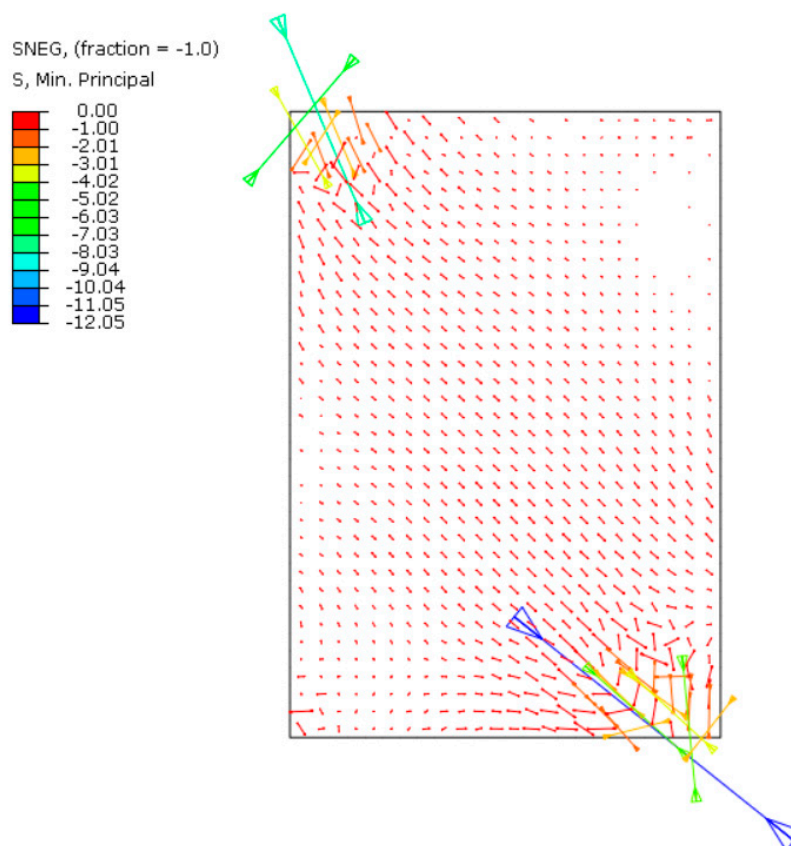


Figure 9. Compressive principal stress distribution in glass elements at the maximum imposed displacement of +45 mm (values in MPa).

4. Fragility Analysis

4.1. Methodology

The fragility analysis was performed for the reference GCW presented in Section 2. Fragility curves can represent a useful tool to assist designers and manufacturers in the design of GCWs, especially for non-customized systems. For example, fragility curves could be used to support designers in the choice of the most suitable system according to the expected seismic hazard. On the other hand, such tools could be applied by manufacturers to investigate the effect of some geometrical features on the expected seismic vulnerability, leading to an improvement in the seismic performance of GCWs. The computational advantage for the derivation of fragility curves was taken from cloud analysis, in which a set of unscaled accelerograms are arbitrarily chosen to carry out a series of non-linear dynamic analyses [16]. The adopted workflow to obtain analytical fragility curves is represented in Figure 10 [17].

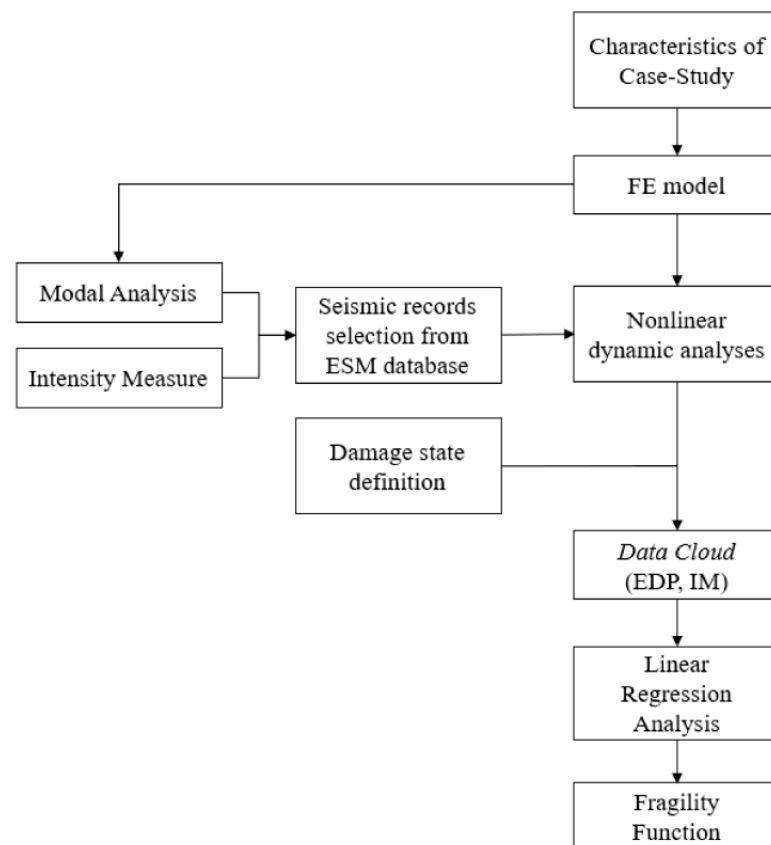


Figure 10. Flow chart of the analytical implementation to develop fragility curves.

First, the numerical model presented in Section 3 was adapted to apply the selected unscaled records at the base of the aluminium frame, as shown in Figure 11. Then, according to Figure 10, a modal analysis was carried out to describe the dynamic features of the GCW, in particular, in terms of natural vibration period (T_1), which is required to select an appropriate range of intensity measure (IM).

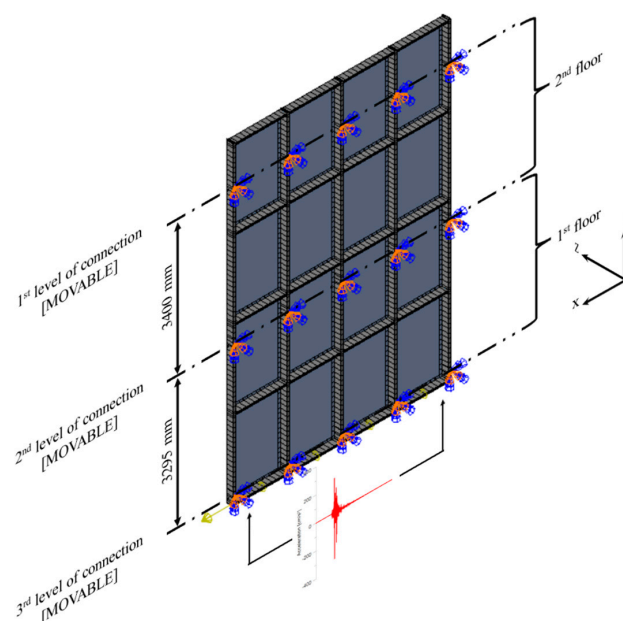


Figure 11. Adaptation of the present numerical model in ABAQUS v. 6.14 [13] for fragility analysis based on time history simulations with input base accelerometer.

The first two modal shapes of the examined GCW are depicted in Figure 12. It is noteworthy that the presence of the glass elements slightly affects the modal shapes and the frequencies of the bare frame for the two lower modes. However, the impact of glazed components becomes increasingly significant when considering higher modes. In detail, a slight increase in the natural frequency (+3%) was recorded in presence of glass components for the first mode, while a progressive decrease was observed for the higher modes, as summarized in Table 5.

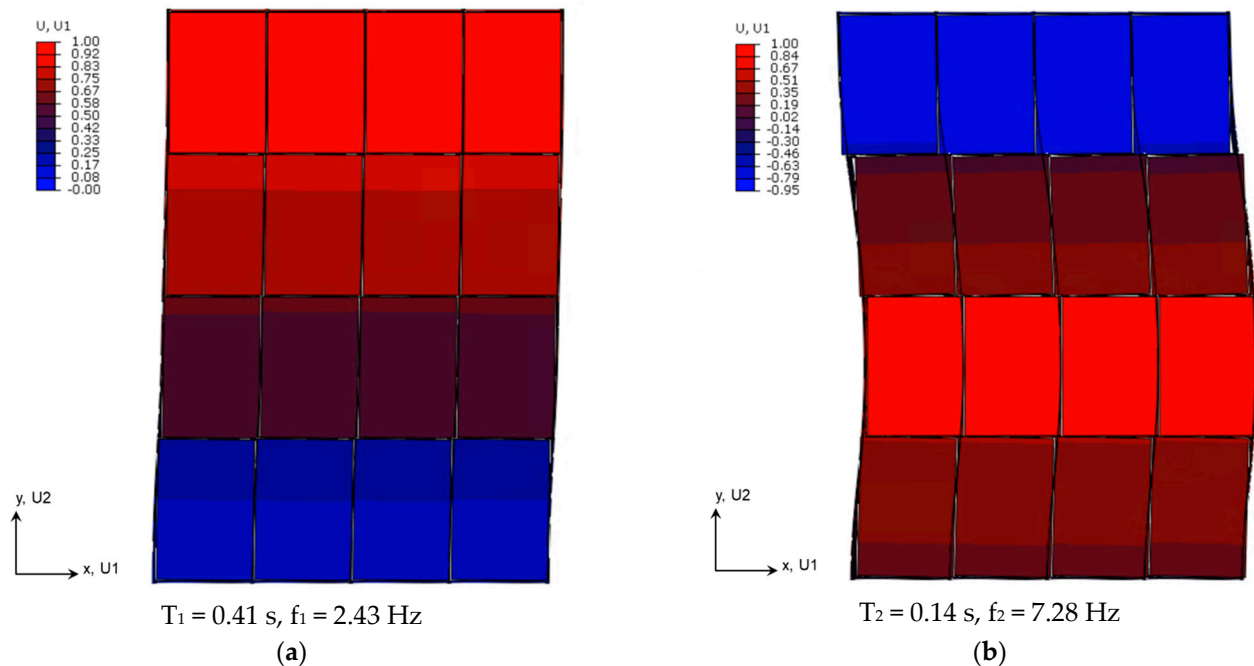


Figure 12. Fundamental vibration frequencies and shapes of the examined glass facade in ABAQUS v. 6.14 [13]: (a) first and (b) second modal shapes.

Table 5. Comparison of numerical vibration frequencies for the glass facade and the bare frame (ABAQUS).

Mode	Frequency [Hz]		Difference [%]
	Glass Facade	Bare Frame	
1	2.43	2.35	+3.09
2	7.28	7.36	−1.02
3	12.59	21.37	−41.09
4	15.71	27.99	−43.88
5	16.01	42.97	−62.75

The set of ground motion records employed to perform non-linear dynamic analyses was selected from the European Strong-Motion (ESM) database [18] in such a manner to ensure an appropriate distribution of cloud data. Based on the limit state criteria and the requirements of the reference seismic standards, a threshold value was defined for each selected engineering demand parameter (EDP) to describe the considered damage state.

Finally, fragility curves represent the probability that the seismic response of the examined component exceeds a prescribed damage state (i.e., EDP threshold associated to a specific limit state) as a function of the earthquake intensity parameter (IM). Fragility curves are defined by means of the cumulative distribution function (CDF) as follows:

$$FC(IM) = 1 - \phi\left(\frac{\ln(EDP_0) - \ln(\overline{EDP})}{\beta}\right) \quad (3)$$

where IM corresponds to the intensity measure, ϕ denotes the standard normal cumulative distribution function, EDP_0 represents the damage state (i.e., the EDP threshold), \overline{EDP} is the median value derived from linear regression analysis as $\ln(\overline{EDP}) = A \cdot \ln(IM_i) + B$ where A and B represent the slope and intercept of linear fit, respectively, and, finally, β is the logarithmic standard deviation calculated as square root of the estimate of the sampling variance:

$$\beta = \sqrt{\sum_{i=1}^m \frac{(\ln(EDP_i) - \ln(\overline{EDP}))^2}{m-2}} \quad (4)$$

where m is the number of analyses performed, and EDP_i represents the EDP value obtained for the i -th analysis.

4.2. Selection of Input Ground Motion and Intensity Measure

As a general approach, the seismic action is characterized by three translational components, two horizontal and one vertical (only in specific cases), that are considered mutually independent [5,6]. In the current standards, attention is primarily given to the IDR amplitude caused by seismic action, as first parameter for the verification of brittle “non-structural elements” like GCWs [5,6]. This also corresponds to the classical setup for experimental studies on facades [4,19,20]. For this reason, in the present study, attention was paid to the effects of horizontal in-plane loads only because of their primary importance in the design of GCWs. In this respect, further investigations could concern the effect of other components of the seismic action and the interaction between the primary structure and the facade. In detail, two different variables representative of the seismic intensity were considered, namely, the peak ground acceleration (PGA) and the spectral acceleration corresponding to the fundamental period of the system ($S_a(T_1)$). To investigate the record-to-record variability in structural response and minimize intrinsic randomness errors, a set of 60 unscaled accelerograms were taken into account to perform the cloud analysis. To minimize the influence of local effects, soil classes A and B (EC8 classification [6]) were taken into account, thus corresponding to rock and very dense sand or very stiff clay soils, respectively. Moreover, an epicentral distance (R) smaller than 50 km was adopted for the selection of input signals. The ranges of seismic events used in terms of $S_a(T_1)$ and PGA were chosen, as also shown in Figure 13, and are equal to 0.31–13.40 m/s^2 and 0.59–6.52 m/s^2 , respectively. The distribution of IM parameters for the selected set of 60 accelerograms is summarized in Figure 13. It can be noted that the histogram shapes are reminiscent of a lognormal distribution, which is generally the most appropriate model for the representation of a seismic dataset.

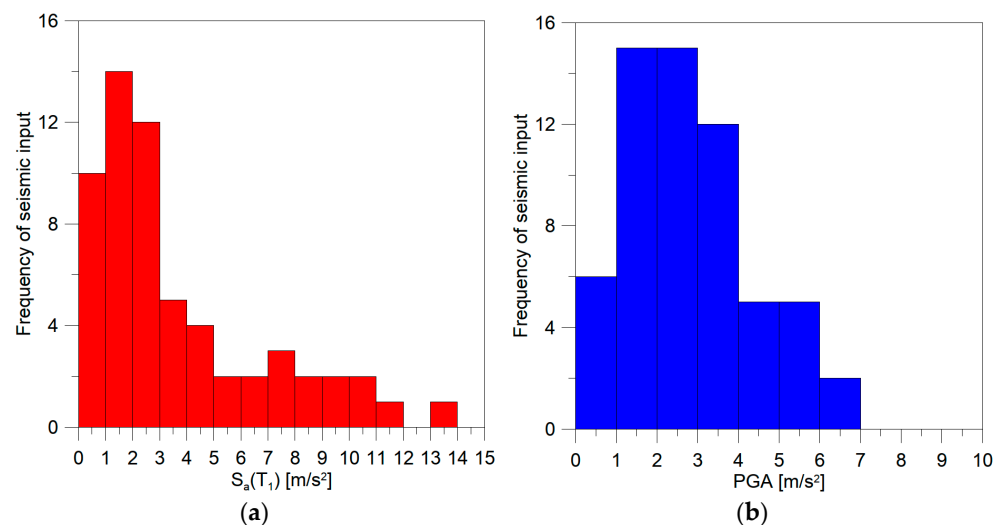


Figure 13. Frequency distribution of seismic input in terms of (a) $S_a(T_1)$ and (b) PGA.

4.3. Definition of Engineering Demand Parameter Thresholds

A crucial step for the definition of fragility curves with the adopted analytical method is the identification of suitable performance variables for the examined system and, thus, the establishment of damage thresholds. For the fragility assessment of the considered GCW, further complexity was found to derive from the absence of technical knowledge about reference performance indicators. Existing regulations, including the EC8 [6] and the Italian NTC2018 [5], classify GCW systems as “non-structural elements”. Therefore, they are required to accommodate the relative seismic displacements of the primary structure. Similar recommendations can be also found in the Italian CNR-DT 210 technical document for structural glass [21], according to which non-structural elements are required to absorb the deformations of the primary structure under the design seismic action. A simple standardization of such a design requirement takes the form of a limitation on relative deformation of floors due to a seismic action characterized by a higher probability of occurrence. Typical reference values are reported in Table 6 in the form of maximum allowable inter-storey drift ratio (IDR/h, where h is the storey height) [5,6].

Table 6. Maximum allowable inter-storey drift ratio according to EC8 [6] and NTC2018 [5].

Classification	IDR/h
Brittle non-structural elements	0.0050
Ductile non-structural elements	0.0075
Non-structural elements not interfering with structure deformation	0.0100

An alternative approach is proposed in the American ASCE 7-10 [3]. It requires that the in-plane horizontal relative seismic displacement at which glass fallout from the GCW occurs, $\Delta_{fallout}$, meets the following requirement:

$$\Delta_{fallout} \geq \max(1.25 \cdot I_e \cdot D_p; 13 \text{ mm}) \quad (5)$$

where I_e represents the importance factor, and D_p denotes the relative seismic displacement that the component is designed to accommodate. It should be noted that the drift causing glass fallout shall be determined in accordance with AAMA 501.6 [4] or by engineering analysis. Moreover, D_p is not required to be taken as greater than the following:

$$D_p = \frac{(h_x - h_y) \cdot \Delta_{aA}}{h_{sx}} \quad (6)$$

where $h_x - h_y = 1926 \text{ mm}$ corresponds to the height of the glass component under consideration, $\Delta_{aA} = 0.020h_{sx}$ denotes the allowable story drift and h_{sx} denotes the story height.

In addition, according to ASCE 7-10 [3], glass with sufficient clearances from its frame such that physical contact between the glass and frame will not occur at the design drift, as demonstrated by Equation (7), need not comply with the requirement of Equation (5):

$$D_{clear} = 2 \cdot c_1 \cdot \left(1 + \frac{h_p \cdot c_2}{b_p \cdot c_1} \right) \geq 1.25 \cdot D_p \quad (7)$$

where D_{clear} represents the relative horizontal displacement that causes initial glass-to-frame contact, $h_p = 1926 \text{ mm}$ and $b_p = 1321 \text{ mm}$ correspond to the height and width of the glass panel, respectively, while $c_1 = c_2 = 6 \text{ mm}$ corresponds to the average of the clearances between the vertical and horizontal glass edges and the frame, respectively. It is worth mentioning that the reference facade does not comply with the glass–frame clearance requirement set out in Equation (7) if D_p is calculated in accordance with Equation (6).

Similarly to the EC8 [6] and the NTC2018 [5] approaches, the Japanese JASS14 [22] specifies a maximum value of drift capacity of a given facade element in relation to the

inter-storey height, the severity of the seismic event and the probability of occurrence. Typical values are reported in Table 7.

Table 7. Reference limitations based on according to JASS14 [22].

Probability of Occurrence	IDR/h
Level 1—Frequent earthquakes	1/300
Level 2—Large-scale earthquakes happened in the past	1/200
Level 3—Severe earthquakes	1/100

Finally, the New Zealand NZS 1170.5 [23] advises that non-structural components should be designed to sustain the actions resulting from the relative deflections that occur for the limit state being considered. More precisely, the ultimate limit state inter-storey deflection shall not exceed 2.5% of the corresponding storey height, while for the serviceability limit state, the inter-storey deflection should be limited so as not to adversely affect the required performance of other structure components. It should be noted that components representing a hazard to life (i.e., with a weight more than 10 kg and able to fall more than 3 m onto a publicly accessible area) shall be verified according to ultimate limit state requirements. According to the above-mentioned regulations, the IDR thresholds shown in Table 8 were considered for the evaluation of fragility curves.

Table 8. IDR thresholds.

Regulation	IDR/h	1st Floor Limit [mm]	2nd Floor Limit [mm]
EC8/NTC2018	0.005	16.5	17.0
ASCE 7-10	0.020	65.9	68.0
JASS14	0.010	33.0	34.0
NZS 1170.5	0.025	82.4	85.0

It is important to highlight that the methodology proposed by the ASCE 7-10 [3] is markedly distinct from the other approaches previously discussed. Indeed, the IDR limitation is not sufficient, as it is for other regulations, to ensure the absence of damage or, more generally speaking, to meet the design standard requirements. In the context of the present study, the allowable story drift provided by the ASCE 7-10 [3] for structures in Risk Category I or II was considered.

4.4. Cloud Analysis Results

The major outcomes from the parametric numerical analyses are shown in Figures 14–16, alongside the linear fits and selected threshold values. It is important to note that the variability in the IDR limits for a given glass system may vary depending on the technical document used for verification. It is additionally noteworthy that the numerical simulations led to stress peaks in the glass elements that were markedly lower than the reference strength, as shown in Figure 15, for the maximum principal tensile stress.

The maximum stress peak recorded for the 60 parametric numerical analyses is approximately equal to 7.5 MPa. In this regard, the characteristic tensile strength of the glass elements was calculated in accordance with the following formula, adapted from [21,24], assuming that the verification is carried out close to the edge:

$$f'_{g;k} = k_{mod} \cdot k_e \cdot k_{sf} \cdot \lambda_A \cdot \lambda_I \cdot f_{g;k} \quad (8)$$

where $f_{g;k} = 45$ MPa is the nominal characteristic value of the tensile strength of annealed glass, $k_{mod} = 1$ is the reduction factor that depends on the load duration and the environmental conditions, $k_e = 0.8$ is a strength reduction factor depending on the edge finish of the glass element and on the distance from the edge of the point at which the strength is calculated, $k_{sf} = 1$ is a strength reduction factor depending on the surface conditions of the

glass, $\lambda_A = 1$ is a scale factor which considers the area subjected to the maximum stress and $\lambda_l = 1$ is a scale factor for the stress near the element edge.

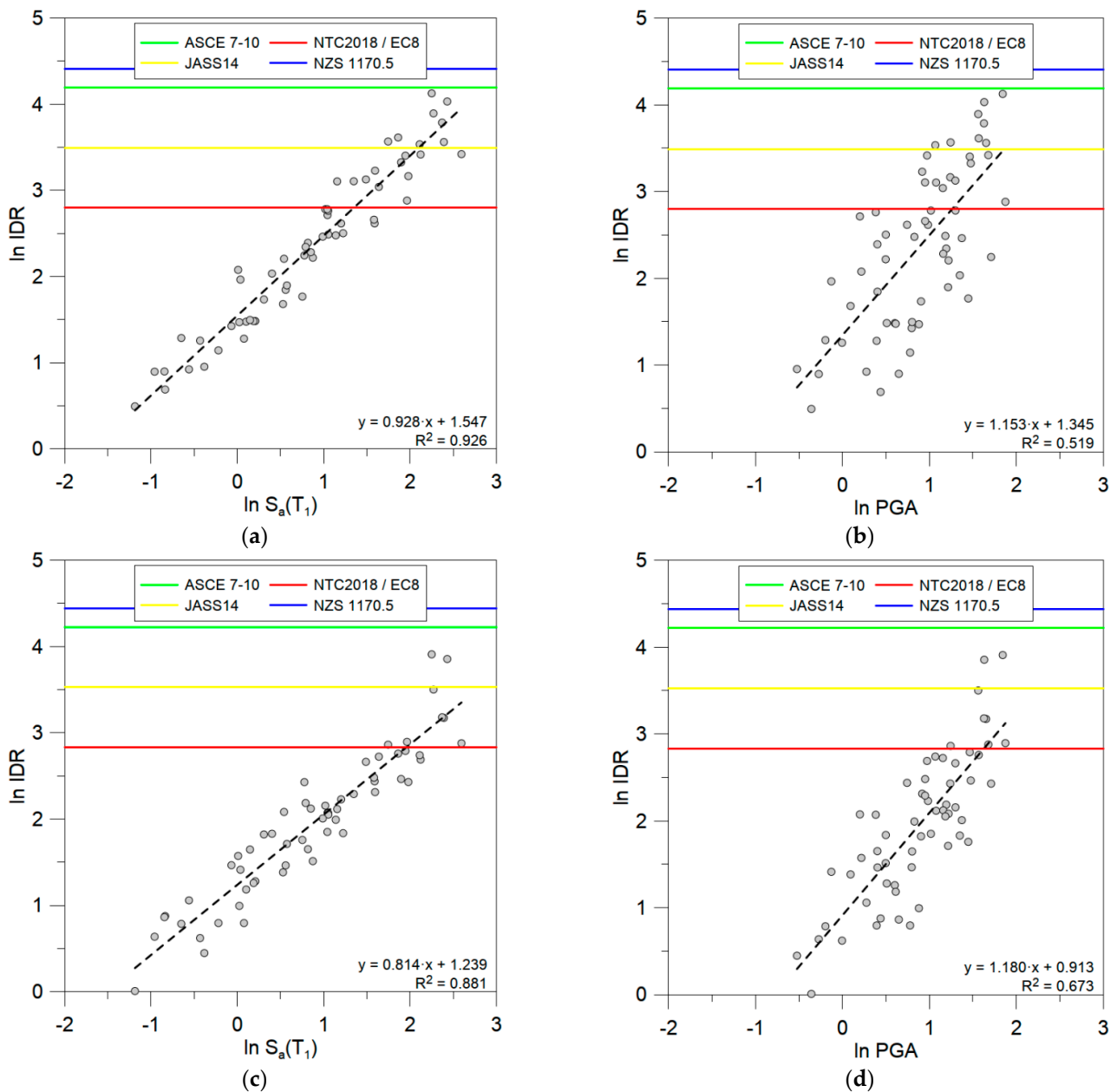


Figure 14. Cloud analysis results: (a,b) 1st-floor and (c,d) 2nd-floor IDR as a function of seismic input variability in terms of $S_a(T_1)$ and PGA.

Further considerations can be drawn from the analysis of the connector outputs. Figure 16 shows the maximum relative displacement of the connectors (CU1) as determined by the FE numerical analyses, as a function of $S_a(T_1)$ and the PGA, respectively. Two distinct displacement thresholds were taken into account: the higher value represents the clearance closure (i.e., a relative displacement equal to the six mm clearance) and thus the contact between the aluminium frame and the glass, while the lower value denotes the yielding of the gaskets (i.e., a relative displacement in accordance with the elastic–plastic model in Figure 3c,d).

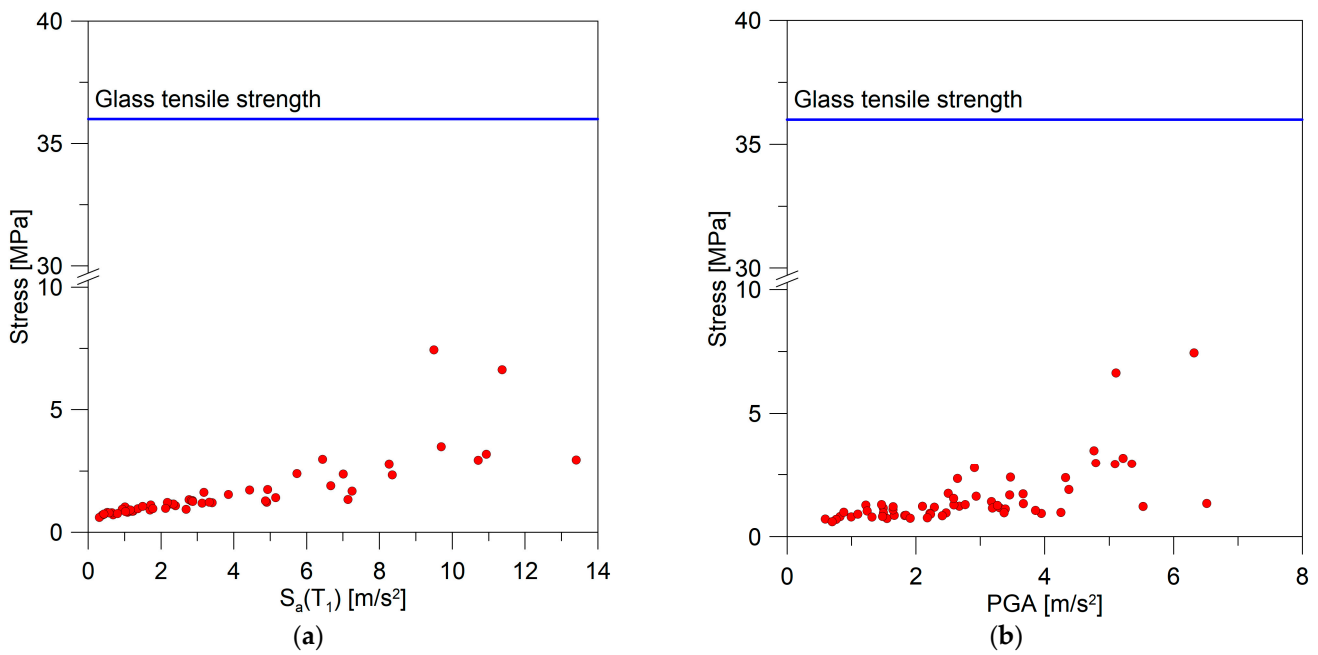


Figure 15. Principal tensile stress peaks in glass elements as a function of (a) $S_a(T_1)$ and (b) PGA.

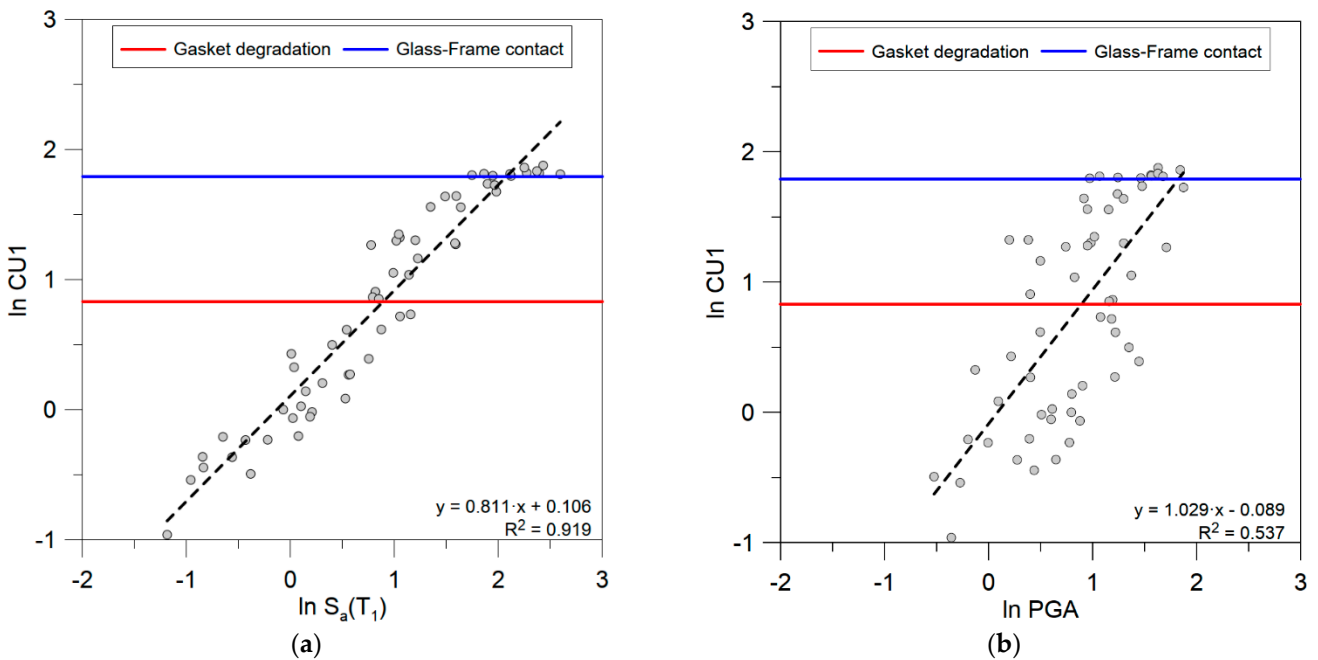


Figure 16. Maximum relative displacement of the connectors (CU1) as a function of (a) $S_a(T_1)$ and (b) PGA.

4.5. Derivation of Fragility Curves

In conclusion, fragility curves were derived in terms of the EDP thresholds corresponding to specific drift limits or relative displacements. Both the PGA and $S_a(T_1)$ values were used as alternative intensity measures on the x -axis of the fragility curves. The obtained fragility curves are proposed in Figures 17 and 18.

In Figure 17, it is possible to note that the use of different threshold limits derived from design standards in the literature has a significant effect on the resulting fragility estimates. As shown, the performance limits provided by EC8 [6] and NTC2018 [5] standards result in the most severe fragility curve for the reference system, while the NZS 1170.5 [23] limit condition is associated with less conservative predictions. This effect is mainly

evident when $S_a(T_1)$ is used as IM, while, for fragility estimates in terms of the PGA, a less pronounced scatter can be observed.

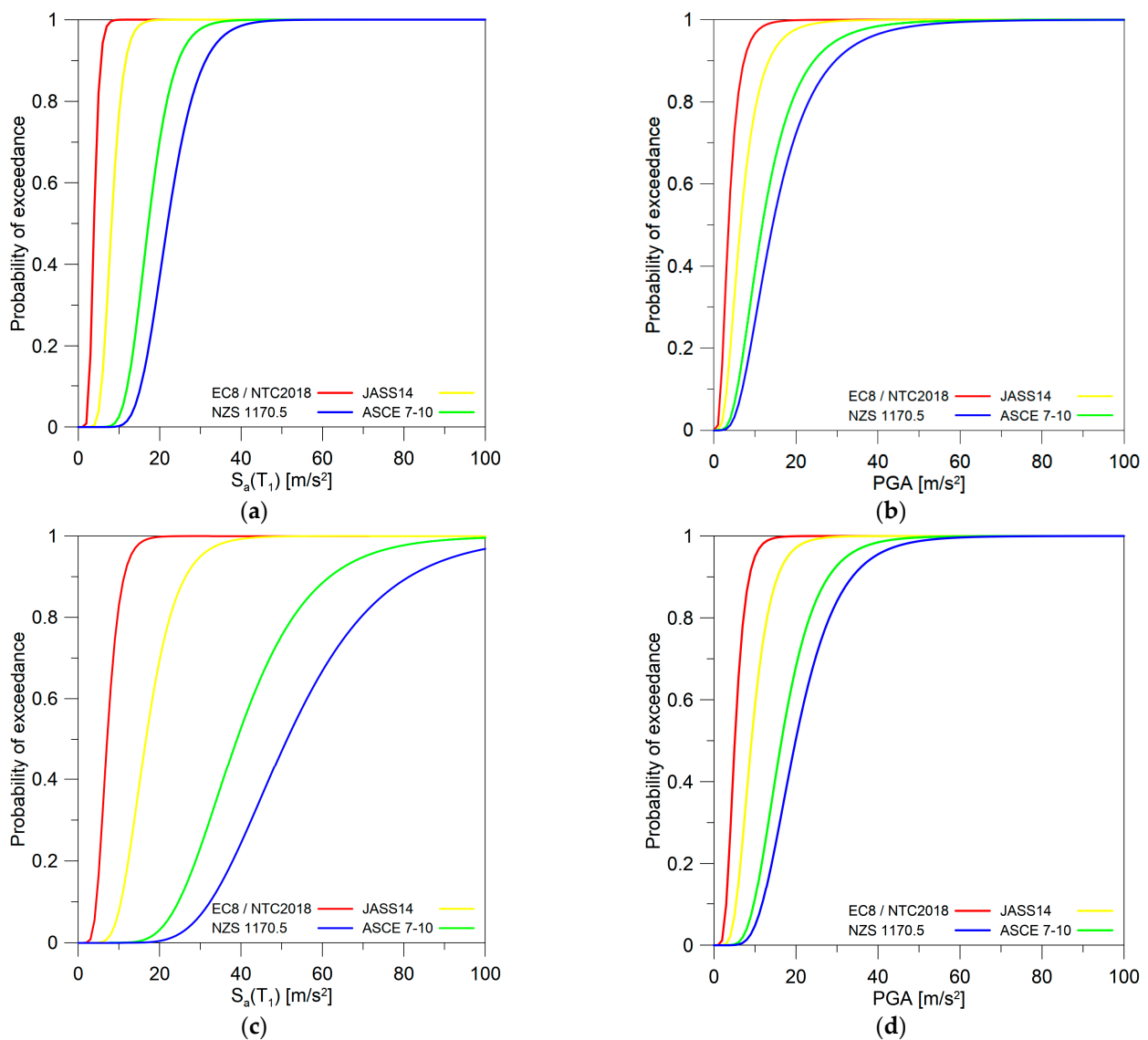


Figure 17. Fragility curves by considering IDRs: (a,b) 1st floor and (c,d) 2nd floor as a function of $S_a(T_1)$ and PGA.

To facilitate a more comprehensive understanding of the seismic performance of the system and enable a meaningful comparison with existing design recommendations, it is beneficial to discuss the numerical results in terms of seismicity levels and associated PGA ranges. In this regard, the PGA values considered in Tables 9 and 10 correspond to the four zones representative of the different hazard levels in the Italian scenario [25]. The aggregated results presented in Tables 9 and 10 demonstrate that a minimal level of seismic damage can be expected even in the event of a high-intensity measurement (Seismic Zone 1, $\text{PGA} = 0.35 \text{ g} = 3.43 \text{ m/s}^2$). It is noteworthy that there is a significant discrepancy in the probability of damage when different drift limits are employed. For example, in comparison to the New Zealand standard, Eurocode [6] and the Italian building code [5] indicate an 80-fold increase in the likelihood of damage to the first floor (Table 9). It is also interesting to observe that for the upper and lower boundaries of the medium seismicity range, specifically Seismic Zone 2 ($\text{PGA} = 0.25 \text{ g} = 2.45 \text{ m/s}^2$) and Seismic Zone 3 ($\text{PGA} = 0.15 \text{ g} = 1.47 \text{ m/s}^2$), respectively, the probabilities of exceedance for the first floor,

as derived from the EC8 standard [6], are approximately 26% and 6%. For the second floor, the probabilities are even lower, at approximately 4% and 0.2%, respectively.

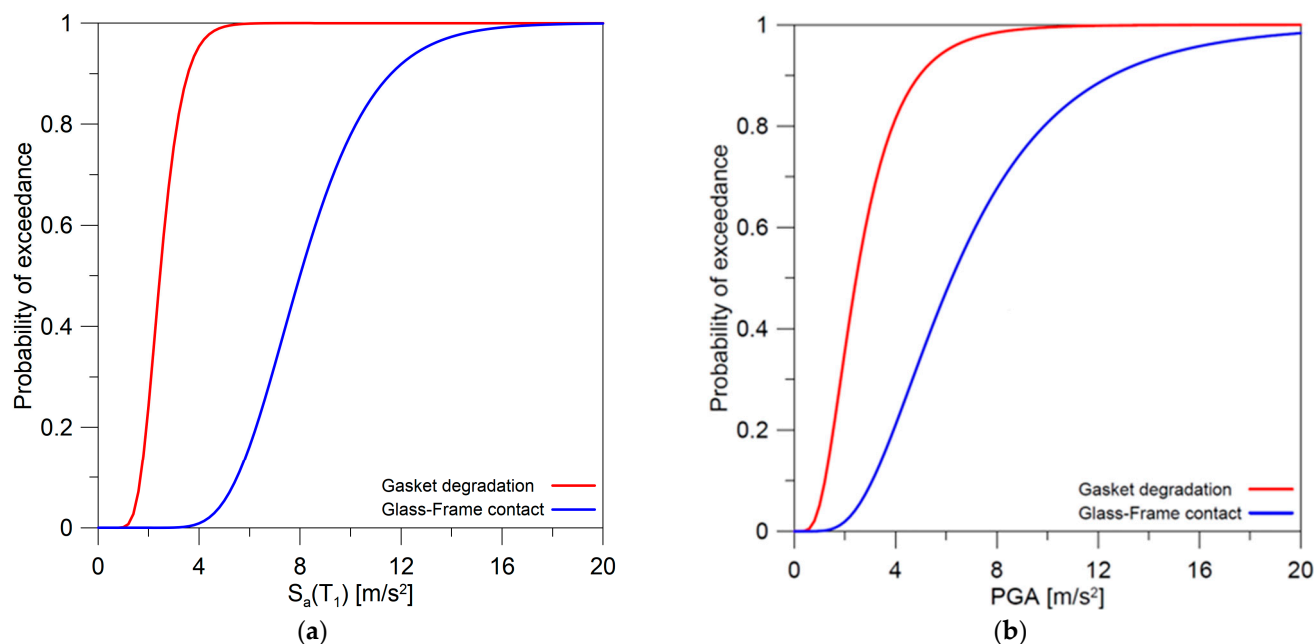


Figure 18. Fragility curves by considering CU1 as a function of (a) $S_a(T_1)$ and (b) PGA.

Table 9. Expected damage probability for the 1st floor as a function of the four seismic zones of the Italian scenario.

Seismic Input		Design Standard			
Zone	PGA	EC8/NTC2018	ASCE 7-10	NZS 1170.5	JASS14
1	0.35 g	47.84%	1.49%	0.60%	13.27%
2	0.25 g	25.88%	0.28%	0.09%	4.39%
3	0.15 g	6.09%	0.01%	0.00%	0.46%
4	0.05 g	0.02%	0.00%	0.00%	0.00%

Table 10. Expected damage probability for the 2nd floor as a function of the four seismic zones of the Italian scenario.

Seismic Input		Design Standard			
Zone	PGA	EC8/NTC2018	ASCE 7-10	NZS 1170.5	JASS14
1	0.35 g	16.88%	0.01%	0.00%	0.85%
2	0.25 g	3.77%	0.00%	0.00%	0.07%
3	0.15 g	0.13%	0.00%	0.00%	0.00%
4	0.05 g	0.00%	0.00%	0.00%	0.00%

Furthermore, it is of interest to compare the expected seismic inputs required to achieve the same damage probability. As illustrated in Figure 17 and outlined in Table 11, the performance of the two floors exhibits a remarkable disparity. For the lower selected value of probability, an increase in approximately 50% in the intensity of the seismic signal is required by the higher floor to achieve the same expected damage. Moreover, the discrepancy appears to intensify, reaching up to 70% for a higher probability of exceedance. The relevant difference in fragility results between the two floors is due to the adopted numerical setup and the boundary conditions applied at the three levels of connection with the primary structure (see Table 3) that lead to a deformation of the facade not directly proportional to its height, in accordance with the first modal shape (Figure 12a). In this

context, the present results suggest that different levels of vulnerability can be expected for different portions of the same stick system and that, for design purposes, the use of an accurate FE model should be preferred to a simpler, but not optimized, inter-storey relative displacement limitation of the primary structure.

Table 11. Required seismic inputs to obtain selected values of damage probability.

Probability	$S_a(T_1)$ [m/s ²]							
	EC8/NTC2018		ASCE 7-10		NZS 1170.5		JASS14	
	1st Floor	2nd Floor	1st Floor	2nd Floor	1st Floor	2nd Floor	1st Floor	2nd Floor
0.25	3.21	5.57	14.31	30.61	18.19	40.27	6.78	13.06
0.5	3.87	7.10	17.25	39.01	21.94	51.31	8.17	16.63
0.75	4.67	9.04	20.81	49.71	26.45	65.39	9.85	21.21
1	9.17	22.77	40.68	125.44	51.99	166.37	20.28	50.56

Finally, Figure 18 provides some valuable insights about the seismic performance of the reference facade. In consideration of the aforementioned seismic zones within the Italian context, it can be observed that even for the highest hazard level (Seismic Zone 1, $PGA = 0.35 \text{ g} = 3.43 \text{ m/s}^2$), the probability of glass–frame contact is notably low (Table 12).

Table 12. Expected probability of exceedance for gasket degradation and glass–frame contact as a function of the four seismic zones of the Italian scenario.

Seismic Input		Failure Type	
Zone	PGA	Gasket Degradation	Glass–Frame Contact
1	0.35 g	73.09%	13.86%
2	0.25 g	50.05%	4.45%
3	0.15 g	17.58%	0.42%
4	0.05 g	0.17%	0.00%

With regard to gasket degradation, the probability of exceedance is almost five times the calculated value for the clearance closure. These results provide further confirmation that a negligible level of damage can be expected even for high-intensity events.

In this context, the absence of a correlation between the IDR limits proposed by the considered design standards and the stress peaks in glass elements should be further highlighted, as proven in [17]. It can be also stated that the suggested limit values—for the purpose of in-plane seismic analysis—are strongly restrictive for the design of primary structures in which glass facades are employed. In this respect, the refinement of performance limits to obtain improved fragility estimates with regard to glass strength, in terms of the IDR limitation of the primary structure, would require extensive experimental and numerical studies to define reliable and comprehensive threshold values. These findings further emphasise the need to develop a reliable FE approach, which would facilitate the design of optimized and safe GCWs.

Finally, it is important to bear in mind that, in real applications, the deformation of the facade is primarily due to the inter-storey relative displacements of the primary structure subjected to seismic action, as they are generally rigidly connected. This differs from the adopted numerical setup, in which the selected input ground motions were applied at the base of the aluminium frame, disregarding the dynamic features and the consequent effects on the GCW of the main structure. The motion at the base of the building is in fact filtered by the response of the construction, in relation to its dynamic characteristics (eigen frequencies) and the height at which the non-structural element is located (modal shapes). It is evident that this interaction could have a significant impact on the fragility results obtained, particularly in relation to the features of the primary load-bearing structural

system and the type of connection provided. In addition, only the effects of horizontal in-plane seismic loads were addressed in this study, neglecting the effects of other components of seismic action that could have a major effect on fragility estimates.

5. Conclusions

Glass curtain walls (GCWs) are vulnerable building components due to the characteristic brittle behaviour of glass. Hence, specific tools are required for the design of safe and optimized systems, especially under extreme actions.

The present study aimed to contribute to the enhancement of finite element numerical approaches for the prediction of the in-plane seismic behaviour of glass facades and to obtain fragility analysis results for the performance-based design (PBD) process.

We initially focused on the description of an optimized numerical modelling strategy for the evaluation of the in-plane seismic performance of a reference case study system. The numerical results, compared to the experimental data and a more refined approach, highlighted the following:

- The robustness and applicability of the present approach for the numerical prediction of the global in-plane seismic behaviour of stick systems in terms of the force–displacement curve;
- The approach’s weak ability to accurately predict energy dissipation under cyclic loads, as a consequence of the major modelling simplification of gaskets;
- Its ability to replicate the glass–frame interaction when the facade is subjected to horizontal in-plane displacements, namely, the deformation (translation and rotation) of the glass panels within the supporting frame;
- The possible applicability of the simplified approach to local performance assessments, especially in terms of the stress peaks in glass elements.

Then, attention was paid to the fragility assessment of the reference glass facade. A major advantage was derived from our use of the cloud analysis in the Cornell’s reliability method, as well as the validated finite element (FE) numerical model for non-linear dynamic simulations.

The results obtained from the non-linear dynamic analyses of the selected structure, as well as from the derived fragility curves, emphasized the following:

- The high variability in inter-storey drift (IDR) limits for a given glass system, depending on the technical document considered;
- The significant effect of the expected structural response of different threshold limits on fragility estimates;
- The typical low stress peaks of glass elements, compared to the nominal material strength;
- The minimum level of damage expected, even in the case of high-intensity events, due to the high flexibility of GCWs.

Most importantly, the present study pointed out the absence of a clear correlation between the IDR limits proposed by the considered design standards and the actual seismic performance of the facade itself. In this regard, the generic limit values that the standards recommend for the IDR ratio limitation approach were overly restrictive, with regard to the real in-plane lateral capacity of the examined GCWs. Such an outcome confirms the need to implement a robust FE modelling approach that allows for the design of safe and optimized glass facade systems.

Author Contributions: N.C.: formal analysis, software, validation, writing—original draft preparation. C.B.: resources, conceptualization, methodology, writing—original draft preparation. All authors have read and agreed to the published version of the manuscript.

Funding: This research activity received no funding.

Data Availability Statement: Data will be shared upon request.

Conflicts of Interest: The authors declare no conflicts of interest.

References

1. Bedon, C.; Zhang, X.; Santos, F.; Honfi, D.; Kozłowski, M.; Arrigoni, M.; Figuli, L.; Lange, D. Performance of structural glass facades under extreme loads—Design methods, existing research, current issues and trends. *Constr. Build. Mater.* **2018**, *163*, 921–937. [[CrossRef](#)]
2. Sucuoğlu, H.; Vallabhan, C.V.G. Behaviour of window glass panels during earthquakes. *Eng. Struct.* **1997**, *19*, 685–694. [[CrossRef](#)]
3. ASCE 7–10; Minimum Design Loads for Buildings and Other Structures. American Society of Civil Engineers: Reston, VA, USA, 2010.
4. AAMA 501.6–01; Recommended Dynamic Test Method for Determining the Seismic Drift Causing Glass Fallout from a Wall System. American Architectural Manufacturers Association (AAMA): Schaumburg, IL, USA, 2001.
5. NTC2018; Aggiornamento delle «Norme tecniche per le costruzioni». Ministero delle Infrastrutture e dei Trasporti: Rome, Italy, 2018. (In Italian)
6. EN 1998–1:2004 Eurocode 8; Design of Structures for Earthquake Resistance—Part 1: General Rules, Seismic Actions and Rules for Buildings. European Committee for Standardization (CEN): Bruxelles, Belgium, 2004.
7. Bedon, C.; Amadio, C. Numerical assessment of vibration control systems for multi-hazard design and mitigation of glass curtain walls. *J. Build. Eng.* **2018**, *15*, 1–13. [[CrossRef](#)]
8. Casagrande, L.; Bonati, A.; Auricchio, F.; Occhiuzzi, A. Dissipating effect of glazed curtain wall stick system installed on high-rise mega-braced frame-core buildings under non-linear seismic excitation. In Proceedings of the COMPDYN 2017, Rhodes Island, Greece, 15–17 June 2017; Volume 2, pp. 3711–3727. [[CrossRef](#)]
9. Caterino, N.; del Zoppo, M.; Maddaloni, G.; Bonati, A.; Cavanna, G.; Occhiuzzi, A. Seismic assessment and finite element modelling of glazed curtain walls. *Struct. Eng. Mech.* **2017**, *61*, 77–90. [[CrossRef](#)]
10. Aiello, C.; Caterino, N.; Maddaloni, G.; Bonati, A.; Franco, A.; Occhiuzzi, A. Experimental and numerical investigation of cyclic response of a glass curtain wall for seismic performance assessment. *Constr. Build. Mater.* **2018**, *187*, 596–609. [[CrossRef](#)]
11. Cella, N.; Bedon, C. Numerical modelling of global/local mechanisms and sensitivity analysis for the seismic vulnerability assessment of glass curtain walls. *Eng. Struct.* **2024**, *319*, 118859. [[CrossRef](#)]
12. Caterino, N. A simplified analytical approach for assessing non-linear in plane seismic response of stick-built glass curtain walls. *Structures* **2023**, *49*, 281–294. [[CrossRef](#)]
13. Simulia. *Abaqus Computer Software*; v. 6.14; Dassault Systems: Providence, RI, USA, 2014.
14. Bedon, C.; Amadio, C. Mechanical analysis and characterization of IGUs with different silicone sealed spacer connections—Part 1: Experiments. *Glass Struct. Eng.* **2020**, *5*, 301–325. [[CrossRef](#)]
15. Bedon, C.; Amadio, C. Mechanical analysis and characterization of IGUs with different silicone sealed spacer connections—Part 2: Modelling. *Glass Struct. Eng.* **2020**, *5*, 327–346. [[CrossRef](#)]
16. Jalayer, F.; Ebrahimian, H.; Miano, A.; Manfredi, G.; Sezen, H. Analytical fragility assessment using unscaled ground motion records. *Earthq. Eng. Struct. Dyn.* **2017**, *46*, 2639–2663. [[CrossRef](#)]
17. Mattei, S.; Bedon, C. Analytical fragility curves for seismic design of glass systems based on cloud analysis. *Symmetry* **2021**, *13*, 1541. [[CrossRef](#)]
18. Luzi, L.; Lanzano, G.; Felicetta, C.; D’Amico, M.C.; Russo, E.; Sgobba, S.; Pacor, F.; ORFEUS Working Group 5. *Engineering Strong Motion Database (ESM) (Version 2.0)*; Istituto Nazionale di Geofisica e Vulcanologia (INGV): Rome, Italy, 2020.
19. Behr, R.A. Seismic performance of architectural glass in mid-rise curtain wall. *J. Archit. Eng.* **1998**, *4*, 94–98. [[CrossRef](#)]
20. Behr, R.A.; Belarbi, A. Seismic test methods for architectural glazing systems. *Earthq. Spectra* **1996**, *12*, 129–143. [[CrossRef](#)]
21. CNR-DT 210/2013; Guide for the Design, Construction and Control of Buildings with Structural Glass Elements. National Research Council of Italy (CNR): Rome, Italy, 2013.
22. JASS14; Japanese Architectural Standard Specification Curtain Wall. Architectural Institute of Japan (AIJ): Tokyo, Japan, 1996.
23. NZS 1170.5:2004; Structural Design Actions, Part 5: Earthquake Actions. Standards New Zealand: Wellington, New Zealand, 2004.
24. prEN 19100-1:2024 Eurocode 10; Design of Glass Structures—Part 1: General Rules. European Committee for Standardization (CEN): Bruxelles, Belgium, 2004.
25. OPCM3274; Ordinanza del Presidente del Consiglio dei Ministri 20 Marzo 2003. n. 3274; Primi Elementi in Materia di Criteri Generali per la Classificazione Sismica del Territorio Nazionale e di Normative Tecniche per le Costruzioni in zona Sismica; G.U. n. 105 del 8 maggio 2003—S.o. n.72. OPCM: Rome, Italy, 2003. (In Italian)

Disclaimer/Publisher’s Note: The statements, opinions and data contained in all publications are solely those of the individual author(s) and contributor(s) and not of MDPI and/or the editor(s). MDPI and/or the editor(s) disclaim responsibility for any injury to people or property resulting from any ideas, methods, instructions or products referred to in the content.